Contents lists available at ScienceDirect

Engineering Fracture Mechanics

Characteristics of dynamic brittle fracture captured with peridynamics

Youn Doh Ha, Florin Bobaru *

Department of Engineering Mechanics, University of Nebraska-Lincoln, Lincoln, NE 68588-0526, USA

ARTICLE INFO

ABSTRACT

Using a bond-based peridynamic model, we are able to reproduce various characteristics of dynamic brittle fracture observed in experiments; crack branching, crack-path instability, asymmetries of crack paths, successive branching, secondary cracking at right angles from existing crack surfaces, etc. We analyze the source of asymmetry in the crack path in numerical simulations with an isotropic material and symmetric coordinates about the pre-crack line. Asymmetries in the order of terms in computing the nodal forces lead to different round-off errors for symmetric nodes about the pre-crack line. This induces the observed slight asymmetries in the branched crack paths. A dramatically enhanced crack-path instability and asymmetry of the branching pattern are obtained when we use fracture energy values that change with the local damage. The peridynamic model used here captures well the experimentally observed successive branching events and secondary cracking. Secondary cracks form as a direct consequence of wave propagation and reflection from the boundaries.

1. Introduction

1.1. Literature review of dynamic brittle fracture

In experiments on dynamic brittle fracture a variety of phenomena are observed (see [1–5]): crack branching (bifurcation of crack), crack-path instability, successive branching events, secondary (or "circumferential") cracking (emerging along the primary cracks at ∼90° angles), asymmetries of crack paths, etc. In a brittle material, cracks propagate rapidly and may curve or split into two or more branches. Under very high states of stress, a propagating crack can generate river-delta crack patterns [1,2]. Cracks propagating in brittle materials can generate fragmentation, which is often the result of a succession of multiple branching events from what was initially a single crack. Moreover, impact experiments on brittle targets reveal radial cracks and circumferential cracks, normal to the radial cracks [6]. In the experiments conducted in [3], waves are shown to generate cracks that propagate normal to the existing crack paths. Interestingly, experimental results on dynamic fracture show that crack paths are not symmetric even if loading conditions and the geometry are (see [1–5]). In this paper we use the peridynamic model to compute solutions to dynamic brittle fracture problems and assess the effectiveness of the simulations in capturing the various characteristic features observed by experimentalists in dynamic brittle fracture events.

Significant efforts have been dedicated to simulate dynamic brittle fracture phenomena over the past several decades. Progress has been made in the last two decades (see, e.g., [7]) and several models are now able to capture some of the characteristics of dynamic brittle fracture. Nevertheless, predicting dynamic fracture in brittle materials is still an open problem and many of the experimentally-observed features of dynamic brittle fracture are not reproduced in simulations unless pre-inserted as special criteria in the model. Three main classes of models have been used to simulate dynamic crack propagation

---

* Corresponding author. Tel.: +1 402 472 8348; fax: +1 402 472 8292.
E-mail address: fbobaru2@unl.edu (F. Bobaru).

Nomenclature

$\boldsymbol{b}$	prescribed bo dy force intensity
c	micromodulus function
D	damage index
E	Young's modulus
$\boldsymbol{f}$	pairwise force function in the peridynamic bond
G_0	energy release rate
H_0	internal subregion
m	ratio between the horizon size and the grid spacing
s, s_0	relative elongation, critical relative elongation
t	time
$\boldsymbol{u}$	displacement vector
$\ddot{\boldsymbol{u}}$	acceleration vector
W	elastic strain energy density
$\boldsymbol{x}$	position vector
α, β, γ	damage stretch coefficients
δ	horizon
$\boldsymbol{\eta}$	relative displacement vector
v	Poisson ratio
ρ	mass density
ω	micro-elastic potential
ξ	relative position vector

in brittle materials: atomistic models (e.g. [8,9]), lattice models (e.g. [10]), and continuum-based models (FEM and XFEM models [7,11–17]). One of the main difficulties of atomistic models in predicting the behavior of dynamic cracks in brittle materials is the size of the simulation: propagation of dynamic cracks is critically influenced by stress waves (e.g. waves reflected from the boundaries of the structure) and atomistic models would be required to simulate the entire structure to capture these waves, a task that currently is impossible to do. In atomistic simulations with absorbing boundaries [18], the crack branching angles are several times larger than the experimentally observed ones [2]. Lattice dynamics models produce ranges of "forbidden velocities" but these are not observed in experiments [10]. In continuum-based approaches, cohesive-zone models modify the local continuum mechanics equations and introduce an internal length-scale related to the cohesive-zone parameters ([7,11–17]). The cohesive-zone Finite Element Method (FEM) or XFEM require a damage criterion and tracking of the stresses around the crack-tip to decide when to insert a branching point at the tip of a crack. In the FEM, the crack advances along the element sides by separating elements from one another, hence the crack path is forced to follow the mesh geometry (see [11–13]). Consequently, the computed crack path deviates from the "correct" crack path and the elastic energy in the systems differs from the actual one. Mesh dependency is a related problem in cohesive-zone FEM-based methods and Zhou and Molinari [15] suggest special mesh refinement strategies to reduce it. The XFEM method ([7]) allows cracks to pass through the finite elements, with some increase in cost for performing integration over the cut elements. The crack path is usually tracked by a level-set function ([7]). With a branching criterion, the method can simulate crack branching in dynamic fracture but it does not predict the experimentally-observed crack propagation speeds unless the material's fracture energy values are modified by a significant factor (see [17]).

A new continuum model, peridynamics, originally designed for modeling dynamic fracture, has been introduced in [19]. Recent results obtained in [20,21] using the bond-based peridynamic model for the crack branching problem show that peridynamics correctly predicts important elements of dynamic crack propagation: the shape of the crack paths, the general profile of the crack propagation speed (similar to the experimental one reported in [22]), attempted and successful branching events (similar to those observed in [2]), and the relation between the way strain energy is delivered into the fracture zone and the evolution of the fracture process (as reported in the experiments in [3,5]). The peridynamic results (the crack propagation speed and the crack path) appeared to converge [20,21] once the horizon (the nonlocal parameter) reached sub-millimeter values. These values may be related to the characteristic length discussed in [2,4].

In this paper, we employ the bond-based peridynamic model, also used in [20,21], and show that the peridynamic model is capable of reproducing more of the dynamic brittle fracture characteristics observed in the experiments mentioned above. We address the issue of crack path stability and branching symmetry and the effects induced by the use of fracture energy that varies with the local damage values. We find the source for small asymmetries of the branched crack paths, in an otherwise perfectly symmetric (about the crack line) computational model, to be in the search algorithm. We obtain successive crack branching events when higher stress levels are reached at the tip of the crack before propagation begins. We also analyze secondary, circumferential-type cracking which develops subsequent to the propagation of the main (radial-type) cracks, as a result of stress waves reflected from the free surfaces. These cracks grow perpendicular to the main cracks.

A specific question we answer here is: "what generates asymmetries of crack paths seen in computational experiments with a, seemingly, perfectly symmetric computational model?". In the actual glass materials, random material variability likely induces the slightly asymmetric crack paths observed in crack branching experiments. In the present study we use homogeneous material models (without material variability, except for the material near the boundaries, which, in peridynamics, has different effective properties than the bulk). The analysis will show that there is a point in the algorithm, related to the list of neighbors and the order of terms in force summations, where symmetry of computation breaks. Once that happens, the slight differences in the build-up of round-off errors influence the crack branching paths and induces small deviations from a symmetric crack path. While not easy to setup, perfectly symmetric computations are possible and they should lead to perfectly symmetric branching events even in the presence of round-off errors (which will preserve symmetry). In the future we will analyze the effect of defects (pores, impurities) and other material inhomogeneities on the crack propagation in dynamic fracture, which is an inherently sensitive dynamic phenomenon.

We also show that strengthening the bonds for nodes that have already suffered some damage, effectively increasing the fracture energy required to propagate a crack in an already partially damaged zone, dramatically enhances the asymmetries in branching and the instabilities in the crack propagation path. Buehler and Gao [23] offered, in an atomistic model context, a possible explanation of crack-path instability by introducing a hyperelastic zone near the crack-tip. They also noted that "*the stronger the stiffening effect, the more rapid the increase of instability speed with increasing value of the critical separation of the atomic bonds*". Interestingly, Buehler and Gao [23] did not use a cubic atomic structure in their computations that would have been symmetric with respect to the crack line. Had they used symmetric computations, relative to the crack path, it would have been easier to see if the stiffening effect in front of the crack-tip would still have resulted in the instability of the crack path. We note that one source for the crack-path instability could be similar to the one explained in Section 3.1, and be due to asymmetric calculations related to the order of terms in force summation calculations. Our results in Section 3.3 show an alternative to that suggested by Buehler and Gao [23] for explaining crack-path instability in dynamic fracture, namely strengthening the material in a damaged zone. In peridynamics, if nothing special is done, the fracture energy required to break a bond in such regions is less than that required for a non-damaged region (in the bulk).

We emphasize that the crack-path instability and crack branching phenomena are different aspects of dynamic crack propagation: the peridynamic results without strengthening of damaged material do show that branching events take place, and they closely replicate experimental results, both in terms of the crack propagation speed profile and the crack path shape (see also [20,21]).

We also analyze the changes taking place in the crack path when higher and higher stress levels are reached just before the crack starts propagating. As the applied loads in our computational model increase in magnitude, branching happens closer to the tip of the pre-crack. Beyond certain stress levels, we obtain successive branching events along each of the main branches. The peridynamic results replicate very well the behavior observed in dynamic fracture experiments [1]. Furthermore, our simulation results indicate that once the crack paths reach the free edges, reflected waves are generated and these waves produce, in turn, secondary cracking with new cracks being generated along, and almost perpendicular to, the faces of the existing cracks. Similar behavior has been observed in dynamic brittle fracture experiments [3,6] as well as in impact on brittle targets simulations where radial and circumferential cracks develop [24].

The paper is organized as follows: in the following section we describe the sample problem setup. In Section 2, we briefly review the peridynamic formulation and describe an approximate way of strengthening bonds depending on the amount of local damage, originally proposed by Silling [25]. In Section 3, we provide evidence that the probable cause for crack branching asymmetry, in a geometrical model that is symmetric about the pre-crack line, is the non-symmetric order of terms in force sums which induces small differences in round-off errors build-up. The inherently sensitive computation of dynamic fracture phenomena amplifies those small differences and this is shown through several numerical results. In Section 4 we analyze the influence of the loading magnitude on crack branching results when higher loading conditions lead to successive branching events. We also investigate the secondary, circumferential-type cracking that takes place due to reflected waves. The conclusions are given in Section 5.

1.2. Problem setup

We consider a thin rectangular plate with dimensions shown in Fig. 1 and a long horizontal pre-notch [2] under remote, symmetric opening loading condition. We apply the loads suddenly and keep them constant during the dynamic simulation. This type of loading generates sharp stress waves (shock waves). All simulation results in this paper are from explicit dynamic analysis in two-dimensions. The brittle material used in numerical tests is Duran 50 glass (also used in the experiments in [26]) with density ρ = 2235 kg/m^3, Young's modulus E = 65 GPa, Poisson ratio ν = 0.2, and energy release rate G_0 = 204 J/m^2.

2. Brief review of the peridynamic formulation

The peridynamic formulation [19] uses integration of nodal forces instead of spatial derivatives in the equations of motion and thus it does not face the mathematical inconsistencies that the classical formulation faces at material discontinuities. Peridynamics is a nonlocal model of continuum mechanics in which material points separated by a finite distance interact with each other. The peridynamic equations of motion at a point $\boldsymbol{x}$ and time t are:
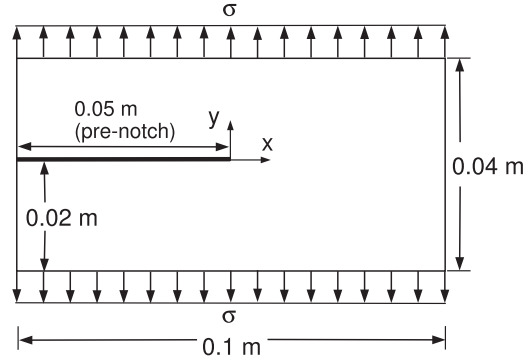
Fig. 1. Geometry and loading conditions for the crack branching problem.

$$\rho \ddot{\boldsymbol{u}}(\boldsymbol{x}, t) = \int_{H_{\boldsymbol{x}}} \boldsymbol{f}(\boldsymbol{u}(\boldsymbol{x}', t) - \boldsymbol{u}(\boldsymbol{x}, t, \boldsymbol{x}' - \boldsymbol{x}) d\boldsymbol{x}') + \boldsymbol{b}(\boldsymbol{x}, t), \tag{1}$$

where $\ddot{\boldsymbol{u}}$ is the acceleration vector field, $\boldsymbol{u}$ is the displacement vector field, $\boldsymbol{b}$ is a prescribed body force intensity, and ρ is mass density. Also, $\boldsymbol{f}$ is the pairwise force function in the peridynamic bond that connects material points $\boldsymbol{x}$ and $\boldsymbol{x}'$. The internal subregion $H_{\boldsymbol{x}}$ (see Fig. 2) is defined as

$$H_{\boldsymbol{x}} = \{\boldsymbol{x}' \in \Re_0 : |\boldsymbol{x} - \boldsymbol{x}'| < \delta\}, \tag{2}$$

where δ is the horizon, the "size" of the nonlocal interaction. Note that no spatial derivatives appear in Eq. (1).

A micro-elastic material [19] is defined when the pairwise force derives from a micro-elastic potential ω:

$$\boldsymbol{f}(\boldsymbol{\eta}, \boldsymbol{\xi}) = \frac{\partial \omega(\boldsymbol{\eta}, \boldsymbol{\xi})}{\partial \boldsymbol{\eta}}, \tag{3}$$

where $\boldsymbol{\xi} = \boldsymbol{x}' - \boldsymbol{x}$ is the relative position and $\boldsymbol{\eta} = \boldsymbol{u}(\boldsymbol{x}', t) - \boldsymbol{u}(\boldsymbol{x}, t)$ is the relative displacement (see Fig. 2) between points $\boldsymbol{x}$ and $\boldsymbol{x}'$. A linear micro-elastic material (the force magnitude depends linearly on the relative elongation magnitude) is obtained if we take

$$\omega(\boldsymbol{\eta}, \boldsymbol{\xi}) = \frac{c(\xi) s^2 \|\xi\|}{2}, \tag{4}$$

where $c(\xi)$ is called the micromodulus function and

$$s = \frac{\|\boldsymbol{\eta} + \boldsymbol{\xi}\| - \|\boldsymbol{\xi}\|}{\|\boldsymbol{\xi}\|}, \tag{5}$$

is the relative elongation of a bond. The corresponding pairwise force is derived from Eqs. (3), (4):

$$\boldsymbol{f}(\boldsymbol{\eta}, \boldsymbol{\xi}) = \begin{cases} \frac{\boldsymbol{\xi} + \boldsymbol{\eta}}{\|\boldsymbol{\xi} + \boldsymbol{\eta}\|} cs, & \|\xi\| \leqslant \delta \\ \mathbf{0}, & \|\xi\| > \delta \end{cases} \tag{6}$$

The micromodulus function is required to satisfy certain conditions of regularity (see [27]), however, the set of allowable functions is quite large. For homogeneous deformations (when s is constant over the entire domain), the relations between
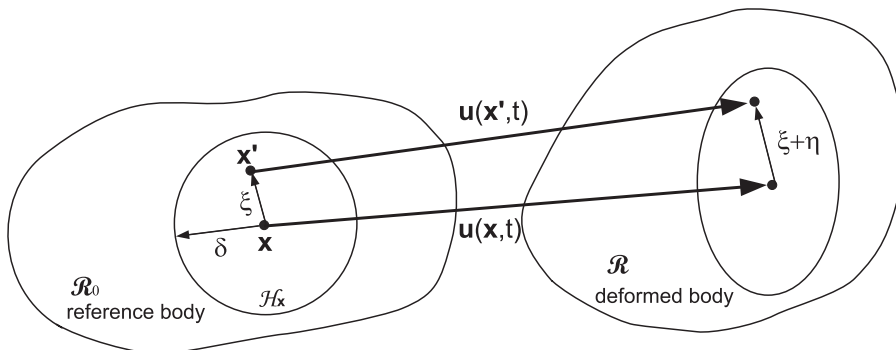

Fig. 2. The deformation of a peridynamic bond.

the elastic material properties and the micromoduli are given in, for example, [25] for 3D, [20] for 2D, and [28] for 1D. Here we use the "constant" micromodulus (see [20]) with the plane stress assumption. For a 2D peridynamic formulation, the elastic strain energy density $W(\boldsymbol{x})$ at a point $\boldsymbol{x}$ is obtained by integrating the micro-elastic potential (Eq. 4) over the horizon region:

$$W(\boldsymbol{x}) = \frac{1}{2} \int_{H_{\boldsymbol{x}}} \omega(\boldsymbol{\eta}, \xi) d\boldsymbol{x}' = \frac{1}{2} \int_{-\delta}^{\delta} \left(\frac{cs^2 r}{2} \right) 2\pi r dr = \frac{\pi}{6} cs^2 \delta^3. \tag{7}$$

To evaluate the micromodulus parameter c in the equation above, we match, for the same homogeneous deformation, the peridynamic strain energy density with the classical strain energy density under the plane stress assumption. The value for the 2D constant micromodulus is then derived as:

$$c = \frac{6E}{\pi \delta^3 (1 - \nu)} \tag{8}$$

where E is the elastic Young's modulus and ν is the Poisson ratio. In the bond-based peridynamics used in this paper, the particles interact only through a pair-potential. This assumption results in an effective Poisson ratio of 1/3 in 2D plane stress and 1/4 in 3D, for an isotropic and linear micro-elastic material [29,30]. This limitation can be removed as shown in [19], and it does not exist in the state-based peridynamics [31].

The micromoduli computed by the formulas shown above are, in fact, obtained for material points inside the bulk, at least a distance δ away from the boundary. If we wanted to match the computed strain energy density for points near the surface, $W(\boldsymbol{x}_{surface})$ with the value for points inside the bulk, $W(\boldsymbol{x}_{bulk})$, then we would get a higher micromodulus value for those points since the integration is performed over a smaller domain. In this paper we keep the micromodulus for the points on or close to the boundary to be the same as that for points in the bulk. This leads to an effectively "softer" material near the boundary. We call this the peridynamic "skin effect". Obviously, as the horizon δ decreases to zero, the skin effect becomes negligible.

In peridynamics, material points are connected via elastic (linear or nonlinear) bonds and each bond can have a critical relative elongation, s_0 [19,25] that models damage. A bond breaks and no longer sustains force when its deformation is beyond this predefined limit s_0. Once a micro-elastic bond breaks, it stays broken. Other types of bonds may be defined based on a potential that depends only on the current relative distance between material points (see [32]). Such potentials are useful in modeling adhesion, for example, where bonds can reform. Because of this damage model, the deformation of a micro-elastic material is history-dependent (see [25]). The critical relative elongation parameter can be obtained by matching with the measured fracture energy as follows: to completely separate a body into two halves across a fracture plane requires breaking all the bonds that initially connected points in the opposite halves (see [25]). The energy per unit fracture length in 2D (or fracture area in 3D) for the complete separation of the body into two halves is the fracture energy, G_0. In 3D, Silling and Askari [25] relate s_0 with this measurable quantity, G_0. In 2D, the connection between the critical relative elongation and the fracture energy is (see [20])

$$G_0 = 2 \int_0^{\delta} \int_z^{\delta} \int_0^{\cos^1(z/\xi)} \left[cs_0^2 \xi / 2 \right] \xi d\theta d\xi dz. \tag{9}$$

For the constant micromodulus given in Eq. (8), we obtain:

$$s_0 = \sqrt{\frac{4\pi G_0}{9E\delta}}. \tag{10}$$

When using a constant s_0 (and if the same horizon δ is used everywhere), we, in fact, have an effectively "weaker" material in regions where damage already happened, or near the boundary (because of the missing bonds). This is similar to the skin effect discussed above, but it involves the strength instead of the stiffness of the material on or near the boundary. The integral used to compute G_0 (Eq. 9) is taken over a smaller region (only the non-failed bonds participate) for points in the damaged region or near the boundary. If we were to impose the same G_0 everywhere, that would result in a higher s_0 for points in the damaged region or near the boundary. In the absence of such a damage-dependent correction for s_0 we effectively have a "weaker" material in front of the crack-tip than in the bulk of the material. Results on dynamic brittle fracture and crack branching are given in [20,21] with a constant s_0 used over the entire domain. The results obtained there show almost perfect symmetry in the way cracks propagate and branch. The symmetry of branching is "helped" by having this effectively-weaker material in the crack-tip area. Note that the peridynamic results, even without any correction for s_0, show branching events that closely replicated experimental results, both in terms of the crack propagation speed and the crack path (see [20,21]). In this paper (see below in Section 3.3) we modify s_0 by increasing it in an approximate way, as suggested by Silling [25]. We then observe the effects this modification has on the crack path and the crack propagation speed.

2.1. Computational details

For the numerical spatial integration of the peridynamic equations above, we use the same algorithm as that described in [25] (mid-point integration). The computational results are all based on uniform grids. In all examples, the ratio between the

horizon size and the grid spacing (the parameter m in [20,21]) is about 4. Reasons for this particular value of m are given in [20] and are based on convergence tests for the crack path in crack branching problems.

Instead of the central-difference time-integration used in [25] we employ the Velocity-Verlet algorithm which is a more numerically stable version of central-differences [33]. A uniform time step size of 25 ns is used for all simulations and this is a stable time step for the Velocity-Verlet scheme with the finest discretization used (horizon $\delta \approx 0.5$ mm and the corresponding grid spacing produced by an m-value of 4.01).

No damping of any kind is used in this study.

The numerical examples shown below are obtained using an in-house 2D serial peridynamic code implemented in Fortran 90/95. All examples are run on a 1.3 GHz Itanium workstation running Linux.

3. Crack-path instability and symmetry-breaking in crack branching

3.1. Sources of crack-path instability in dynamic fracture simulations: round-off errors and slightly asymmetric computations

In previous computations (see, e.g., [20,21]) crack branching paths were not perfectly symmetric about the pre-crack line even if they were obtained with a perfectly symmetric geometry (in [21] the origin of the coordinates system was in center of the sample) and symmetric loading conditions. This section discusses the search for the source of the symmetry-breaking in the, apparently, perfectly symmetric computations. Even in the presence of round-off errors, these errors should be symmetrically distributed about the line of the pre-crack in Fig. 1, and should therefore lead to perfectly symmetric crack branching about the pre-crack line. We shall see that one algorithm in the computations slightly breaks this symmetry. All the computations are performed with grids that have an even number of nodes along the direction perpendicular to the pre-crack line, so that we do not have nodes along the pre-crack line.

In the discrete version of peridynamic formulation, each node has a family of neighboring nodes within its horizon region. In order to find this family for every node, we use the same search algorithm independent of the location of the nodes relative to the pre-crack line. For a uniformly distributed nodal structure, for instance, the list of nodes in the family of node a (see Fig. 3) generated by this algorithm is shown in Fig. 3. The symmetric node about the pre-crack line of node a is node b, with its list of nodes in its family also given in Fig. 3. Notice that the symmetric node of the first family node for node a is not the first node in the list of node b. The order in the family list is important since that defines the order in which the terms are summed up in the numerical approximation of the integral of force densities at a node. The difference in the summation order leads to different values of the round-off errors for pairs of symmetric nodes. These differences grow in time and lead to the observed symmetry-breaking in the crack branching path. This appears to be the only place in our computational algorithm where the symmetry of the computations is broken. To preserve a perfect symmetry in the computations we could, artificially, change the search algorithm for building the family list. Clearly this approach would require special coding for each particular example and geometry and that would not be practical. Obviously, symmetry-breaking in crack branching will be inherent if a non-uniform or random grid is used.

We also performed computations in which the origin of the system of coordinates is not at the center of the sample (coordinates are no longer symmetric with respect to the crack line), and the results showed an increased asymmetry in the crack branching paths. Experimental results on crack branching [1–5], setup with symmetric geometry and loading conditions, show significant asymmetry in the crack branching paths that may be explained by the presence of certain variations in the material or by possible changes in the material behavior that take place near the crack-tip/surfaces. To test this hypothesis, we provide, in Section 3.3, an example of asymmetry induced by specific changes in the fracture energy of material points that have already suffered damage.
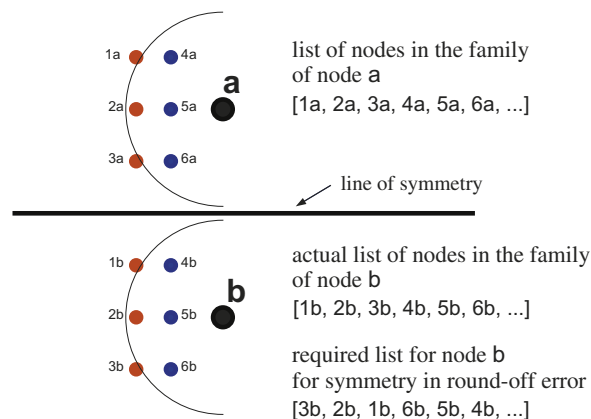

Fig. 3. The root-cause for symmetry-breaking in crack branching: the lists of nodes in the families of two, geometrically symmetric, nodes do not preserve symmetry (the larger circles show part of the horizon for the given node).

We next analyze the build-up of differences in the total vertical displacements for two symmetric nodes about the pre-crack line from Fig. 1. A tensile loading of σ = 12 MPa is applied. Two symmetric nodes about the pre-crack line (a and b) are selected at (x,y) = (0.03 m, ±0.01 m) in the symmetric coordinate system (centered at the center of the plate) seen in Fig. 1. The relative differences between the vertical displacements d_y for these two nodes from the dynamic crack propagation simulation are shown, at different time steps, in Table 1. The absolute values of these displacements are between 3×10^{-6} m and 3×10^{-5} m from 5 to 40 μs. Had the round-off errors been the same, the displacements for these nodes, symmetric about the crack line, would have been exactly the same. As seen from Table 1, however, the round-off errors for the two symmetric nodes are different and these differences grow in time. Moreover, when we use a system of coordinates with its origin located at the bottom left corner ("biased" coordinates) the asymmetries in the round-off errors are significantly larger than those obtained when using the symmetric coordinates. The slight symmetry-breaking in crack branching events computed on a symmetric grid with the two systems of coordinates mentioned above is seen from Fig. 4a and b.

In Fig. 4, we show crack propagation results for three peridynamic simulations for the setup shown in Fig. 1. The results in Fig. 4 are obtained with uniform grids of 404 by 162 nodes. The horizon size is about 1 mm (corresponding to m = 4.01) and the simulations required about 6 h CPU time (covering 50 μs of real time). For all results in this paper, damage is implemented as the fraction between the number of broken bonds and the number of initial bonds [25]. Cracks in peridynamics form as surfaces between material points develop, as a consequence of sequential breaking of bonds. All damage maps, which show the crack paths, in this paper, are using the same color-bar given in Fig. 4a. In the symmetric coordinate system with a loading σ = 12 MPa (see Fig. 4a), even though there are small asymmetries in round-off errors (see Table 1), the crack paths are almost perfectly symmetric. However, when the system of coordinates is placed at the lower-left corner (see Fig. 4b), the asymmetries of crack paths are more visible. As expected, the original asymmetry in the nodal coordinates will build larger differences between displacements of nodes situated symmetrically about the pre-crack line (see also Table 1). We also notice that, under a higher loading, asymmetries are readily visible even for the case when the system of coordinates is placed at the center of the plate (see Fig. 4c). These results show how easily the asymmetries of the crack path become severe in the dynamic brittle fracture simulation with small perturbations. Moreover, we notice that this sensitivity to small perturbations is not related to the crack branching phenomenon but is related to the instability of the dynamic crack

Table 1
Comparisons of vertical displacements for two nodes, symmetric about pre-notch line.

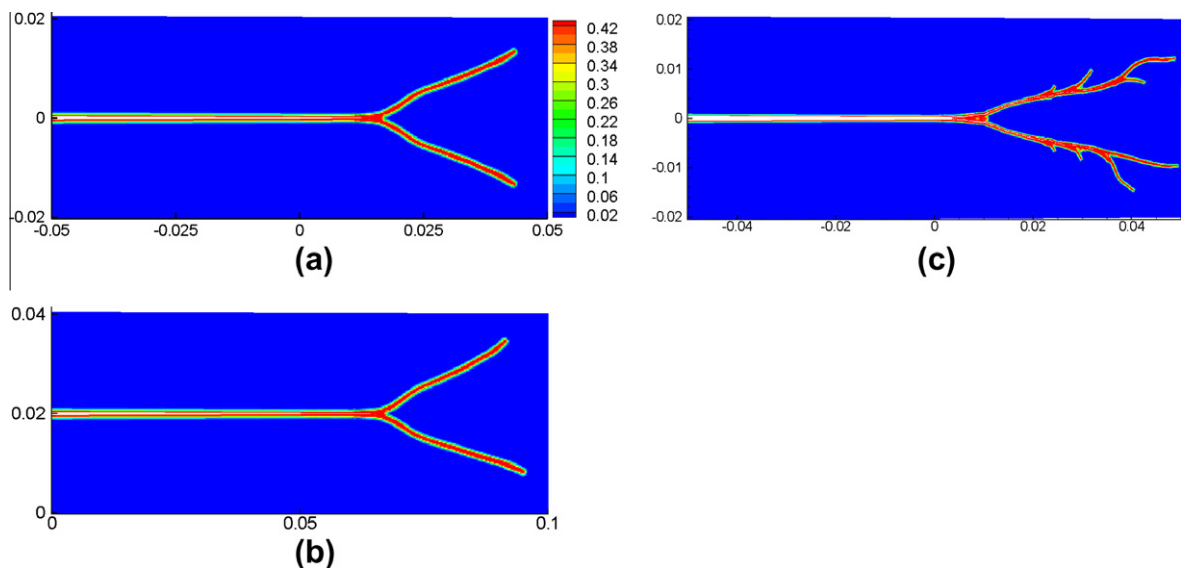| Time step (μs)	Relative difference, $|d_y(\boldsymbol{b})| - |d_y(\boldsymbol{a})|/d_y(\boldsymbol{a})$	
	Symmetric coords.	"Biased" coords.
5	1.2×10^{-6}	5.8×10^{-6}
10	1.6×10^{-5}	3.9×10^{-5}
30	7.0×10^{-4}	8.4×10^{-2}
40	3.6×10^{-3}	7.1×10^{-2}

Fig. 4. Damage maps (crack paths) for three tests of symmetry-breaking and crack-path instability in crack branching: sudden loading on the top and both boundaries with σ = 12 MPa (a, from [21]) at 46 μs and σ = 27 MPa (c) at 38 μs. A symmetric coordinate system was used for results (a) and (c). In (b, from [20]) results from loading of σ = 12 MPa at 46 μs and the system of coordinates centered at the lower-left corner.

propagation. Buehler and Gao [23] also obtain crack-path instabilities in dynamic fracture when, in their atomistic model, a stiffening region (hyperelasticity) is introduced in front of the crack-tip. The close-packed grid used in [23] is not symmetric about the crack line and it would be interesting to know if the crack-path instabilities are still observed on a symmetric atomic lattice (a cubic lattice). Our results with peridynamics show that the addition of hyperelasticity around the crack-tip used in Buehler and Gao [23] is not needed in peridynamics to generate crack-path instabilities. Peridynamics predicts crack branching without any changes to the model, and one source of crack-path instability is round-off errors, the fact that computations cannot be setup perfectly symmetric in general, and the sensitive nature of the dynamic crack propagation. In Section 3.3 we show the dramatic influence exerted on the crack-path instability by performing, for example, small changes, proportional with the amount of damage suffered, on the fracture energy in the crack region.

3.2. Numerical convergence in peridynamics

The nonlocal character of peridynamics leads to two types of numerical convergence ([28]): the results for the dynamic crack branching problem in terms of the crack-path and crack propagation speed. Based on those results, we concluded that a value of m close to about 4 provides solutions that are both efficient and close to the m-converged results. In this paper we use such a value for m. A δ-convergence test is shown below for the damage-dependent model described in the next sub-section (see Fig. 5).

3.3. Influence of strengthening of bonds in damaged regions on crack-path instabilities and symmetry-breaking

As discussed in Section 2, Peridynamic models, in their simplest form, show a skin effect. In principle, one could compute micromoduli for nodes on or near the boundary, which have "missing bonds", to match the strain energy density of the bulk. Such an approach would result in a stiffening of bonds for nodes on or near the boundary compared to bonds in the bulk, and the effective material stiffness would be constant everywhere. However, if one considers smaller and smaller horizons, the skin effect becomes negligible. In this study we keep the micromoduli the same for points in the bulk or on or near the boundary. Instead, because a similar phenomenon takes place for the computation of the critical relative elongation parameter s_0, we choose to "strengthen" the material in damaged regions by increasing s_0 depending on the amount of damage at that node. One could attempt an exact evaluation of the damage-dependent (variable) s_0. However, here we resort to a simpler way, namely an approximation proposed by Silling [25] which is described by the formula below and Fig. 6.

$$s = \begin{cases} s_0 \times min\left[\gamma, 1 + \beta \times \frac{D-\alpha}{1-D}\right], & D > \alpha \\ s_0, & otherwise \end{cases} \tag{11}$$

where the damage index D is defined as the ratio of the number of broken bonds to the number of initially bonds. s_0 and s are the initially given and the modified critical relative elongation parameters. Also, α, β, and γ are damage stretch coefficients: if $\alpha = \beta = 0$ and $\gamma = 1$ we recover the constant s_0 model.

Using the damage-dependent s_0 model with $\alpha = \beta = 0.2$ and $\gamma = 1.4$ (see Fig. 6), the convergence study for the crack branching problem with three different horizons ($\delta \approx 2$, 1, and 0.5 mm) is performed. The results after 46 μs from the start of the simulations are shown in Fig. 7. The result in Fig. 7a is obtained with a coarse horizon ($\delta \approx 2$ mm) and a grid of 203 by 82 nodes, while a fine horizon ($\delta \approx 0.5$ mm) and a fine grid of 803 by 322 nodes were used for the result shown in Fig. 7c. The horizon and grid of for the result in Fig. 7b are the same as those used to get the solutions in Fig. 4. The CPU time for the finest model (50 μs real time) was about 48 h. The symmetric coordinate system (centered at the center of the plate) is employed for the plate with pre-notch (Fig. 1) with Duran 50 glass and a tensile sudden loading of 12 MPa is applied and maintained constant throughout the simulation. In Fig. 7a–c we see similar, but not the same, single-crack branching events. Clear symmetry-breaking takes place and it is interesting to compare this with the result obtained with the damage-independent (constant) s_0 model where symmetry was almost perfect, as shown in Fig. 4a. This indicates that the asymmetries and instabilities of crack paths are enhanced by the increase of s_0 near the fractured surfaces where the material has been already
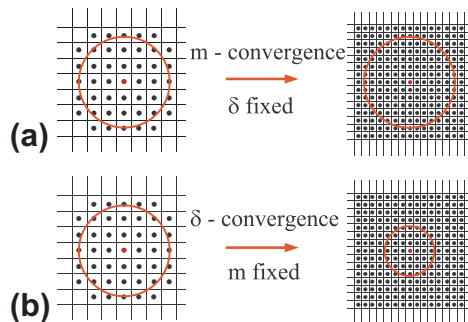

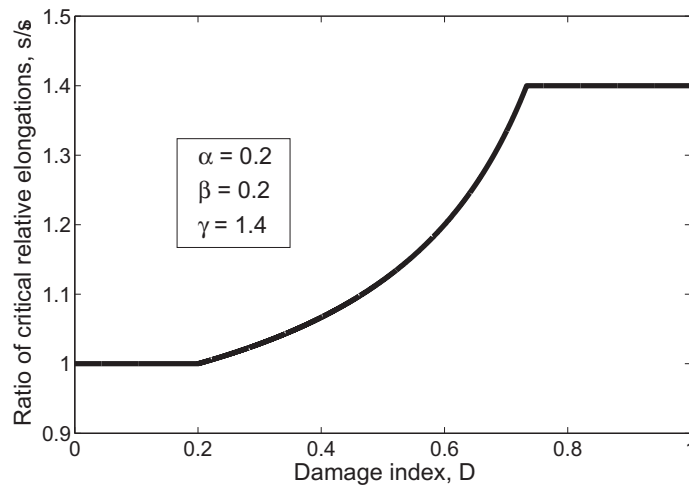**Fig. 5.** Description of (a) m-convergence and (b) δ-convergence.

Fig. 6. Critical relative elongation variation with respect to the damage index.
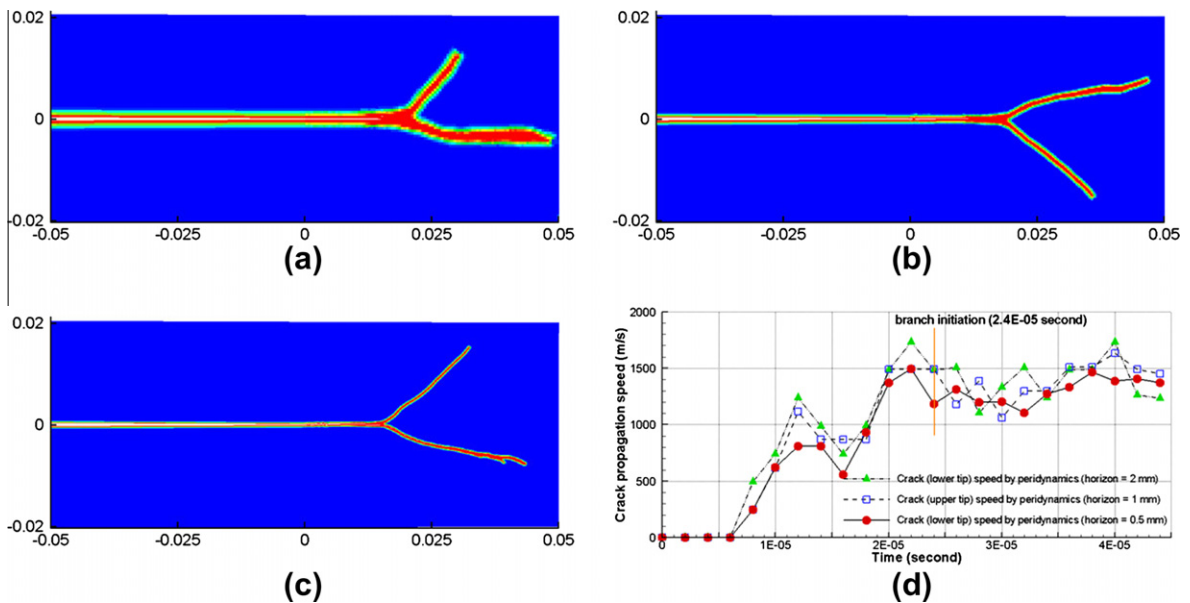

Fig. 7. Asymmetries of crack paths under changing the horizon size (and keeping m fixed) at 46 μs; (a) $\delta \approx 2$ mm, (b) $\delta \approx 1$ mm, and (c) $\delta \approx 0.5$ mm. (d) the δ-convergence for the crack propagation speed profiles (with $\alpha = \beta = 0.2$ and $\gamma = 1.4$ in Eq. (11)).

damaged. In the model with the same s_0 everywhere (the case of Fig. 4a), bonds in the damaged regions are effectively "weaker" then bonds connecting nodes in the bulk and cracks can more "easily" propagate and maintain a certain direction of propagation through these "weaker" bonds. This type of behavior helps in preserving the relative crack path stability and symmetry observed in [20,21].

The longer crack lines in the branched path are tracked for computing the crack propagation speeds: thus we follow the lower crack-tips for the cases in Fig. 7a and c, and the upper crack-tip for the case in Fig. 7b. Even if the branched paths loose symmetry soon after branching, we still find that the crack propagation speed profiles are similar to one another, as shown in Fig. 7d, and these speed profiles are also very close to the results for the fixed s_0, as obtained in [21].

4. Successive branching and secondary cracks

4.1. Successive branching under higher loading levels

The experimental results [1] shown in Fig. 8 feature various patterns of successive branching events that appear when higher stress levels are reached at the crack-tip before the pre-crack starts running. We investigate computationally, with
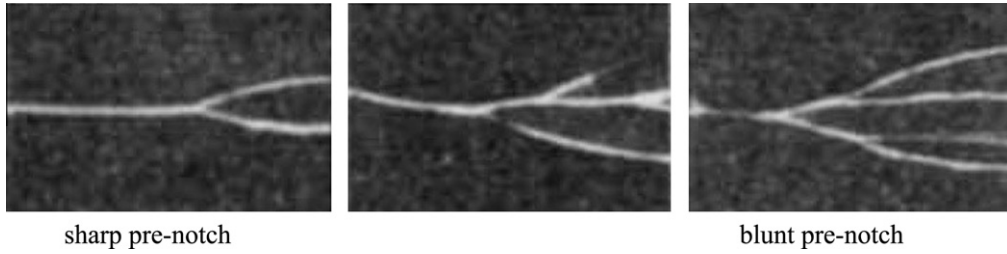
Fig. 8. Experimental results from Bowden et al. [1]. From left to right, the stress intensity factor reached before the crack starts propagating increases as the severity of the pre-notch decreases. The original figures are rotated and cropped for comparison with results in Fig. 9.

the peridynamic model described in Section 2, the effect of the magnitude of the suddenly applied loadings, on the crack patterns. We qualitatively compare the computational results with the experimental results from [1]. Note that the experiments are performed using soda-lime glass. The soda-lime is weaker but slightly stiffer than Duran glass. Peridynamic results using a material similar with soda-lime glass are reported in [20]. Also, the boundary conditions used in the computations here are different from the ones used in the experiments. In experiments, the loading is quasi-static, the sample being loaded slowly until reaching the point when the pre-crack starts running dynamically. We cannot afford an explicit computation over minutes like in the experiments, so we load the sample suddenly, which induces a shock-like wave. Thus, the loading is dynamic in the computations. A possible alternative for the computations is to load quasi-statically up to a point that does not set the crack propagation, and then load dynamically with a small stress pulse, as done in, for example, [17]. This will be tested in the future. For these reasons we do not perform a quantitative comparison between the experiments and the computation, but rather a qualitative one. The geometry is also slightly different: in our simulations we use the configuration with a long horizontal pre-notch and loads applied along the vertical direction (see Fig. 1), which is the setup also tested by Ramulu and Kobayashi [2], but Bowden et al. [1] used a configuration with the pre-notch vertical and running along the short dimension of the plate, and the loading is horizontal.

Because of our dynamic loading, it is easier to obtain secondary branching in the setup of Fig. 1, where the boundaries are closer to the tip of the crack, then in the setup used in [1]. The way a higher stress level is reached in the experiments is by modifying the "severity" of the pre-notch: with a sharp notch the crack starts running at lower stress intensity at the tip of the notch; with a blunt notch a higher stress intensity factor is reached before the crack starts propagating. In our simulations we "mimic" these experimental conditions in the following way: we apply loading pulses of different magnitudes with the lower loading values simulating the lower stress intensity at propagation and the high loading values inducing higher stress intensity at the crack-tip. The comparisons below between the experimental results and our peridynamic simulations are, therefore, only qualitative.
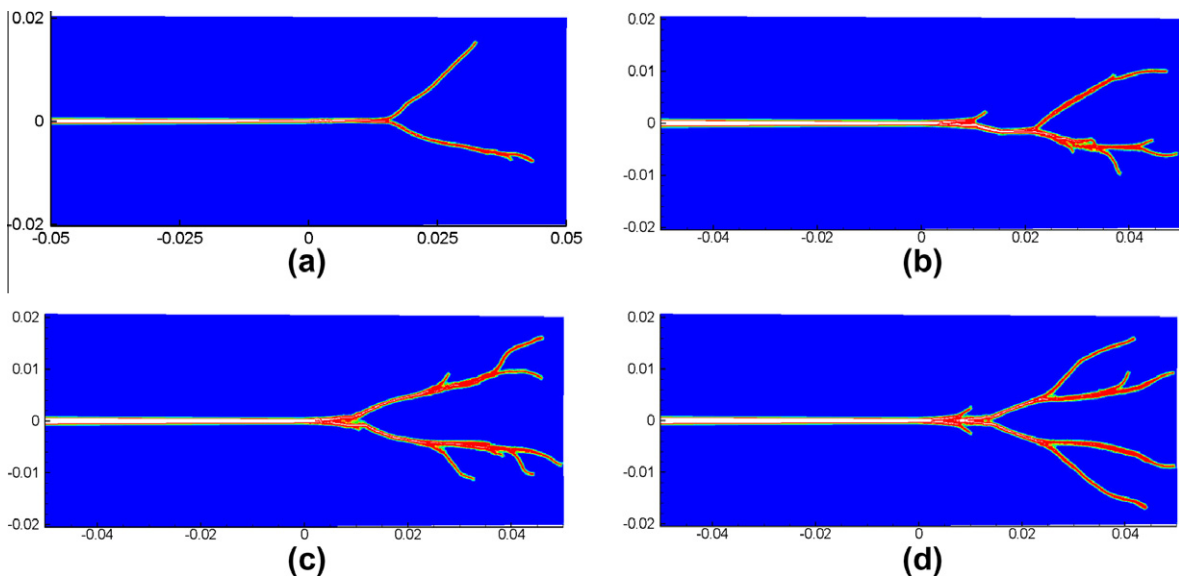

Fig. 9. Peridynamic damage maps (crack paths) under different loading magnitudes for $\delta \approx 0.5$ mm: damage-dependent s_0 model with $\sigma = 12$ MPa at 46 μs (a), $\sigma = 27$ MPa at 38 μs (b), and $\sigma = 32$ MPa at 36 μs (c), and damage-independent s_0 model with $\sigma = 32$ MPa at 36 μs (d).

At the lower stress intensity levels at the start of crack propagation for which applied tensile loadings are less than roughly 12 MPa, the crack runs mostly straight and it does not branch for both the numerical and experimental results. At the higher stress levels, two-way crack branching occurs (see Fig. 9). After an initial branching event, the individual crack branches may also experience branching or may arrest, and they spread over a wider area. These features are also observed in the experimental results (see Fig. 8). As the stress intensity increases, there are many attempted and successful branching events (see Fig. 9). Qualitatively, the peridynamic results match the experimental results seen in Fig. 8. We notice that the damage-dependent s_0 model can enhance asymmetries of the crack propagation (see Fig. 9a–c) but notice that even with the damage-independent s_0 model symmetry-breaking does happen (see Fig. 9d).

We explain the increased crack path dynamic instability in the damage-dependent s_0 model as follows: it becomes easier for the crack path to form to the left or right of the propagation direction at one point since bonds connecting nodes in the areas with non-zero damage may be slightly tougher than bonds connecting nodes in the non-damaged bulk. A similar dynamic instability effect is expected to be seen if, instead of modifying the critical relative deformation of the bonds in
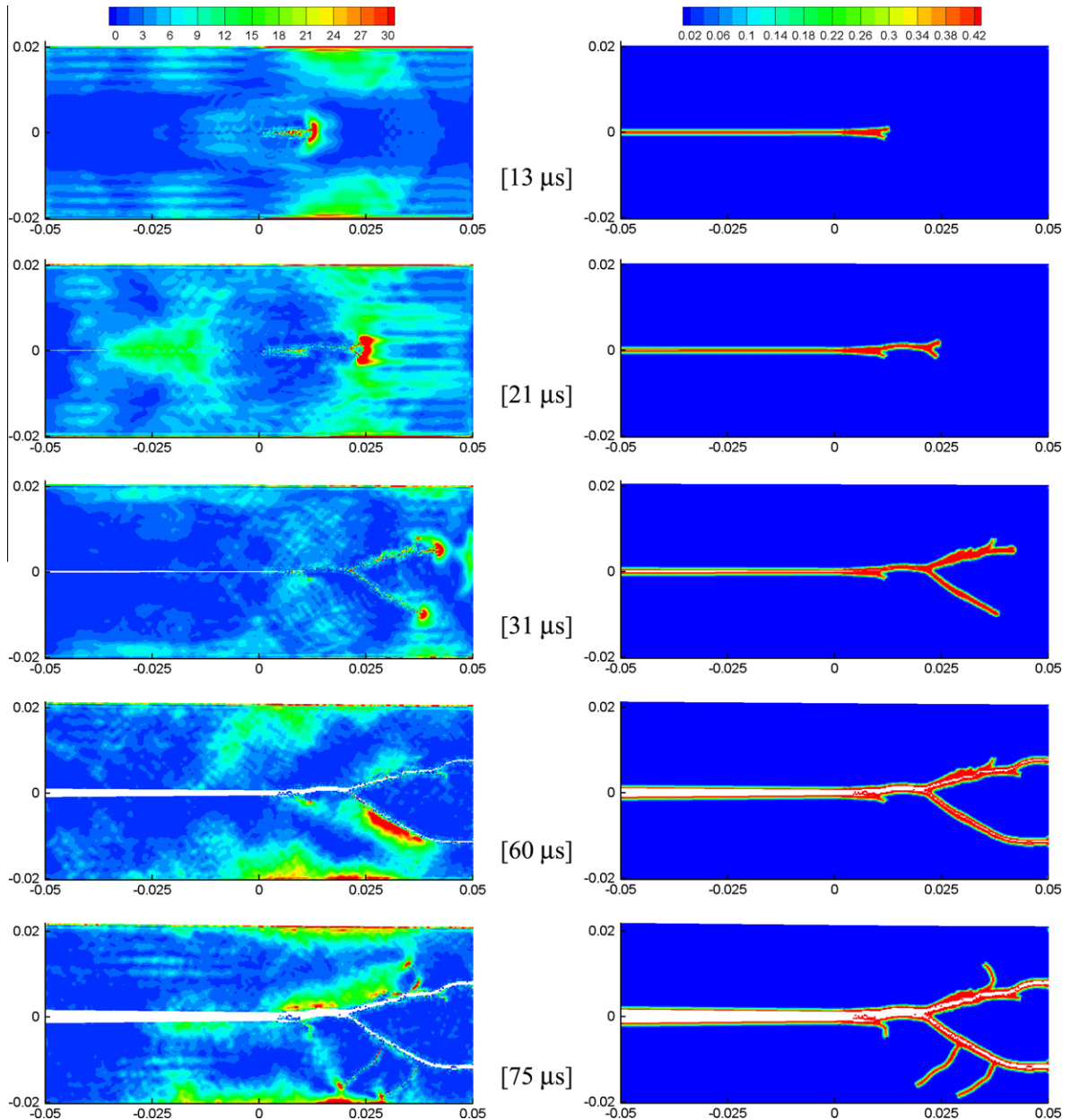

Fig. 10. Elastic strain energy density (left column) and damage maps (crack paths, right column) evolution in time (center column) for a damage-dependent s_0 model, $\delta \approx 1$ mm, $\sigma = 23$ MPa.
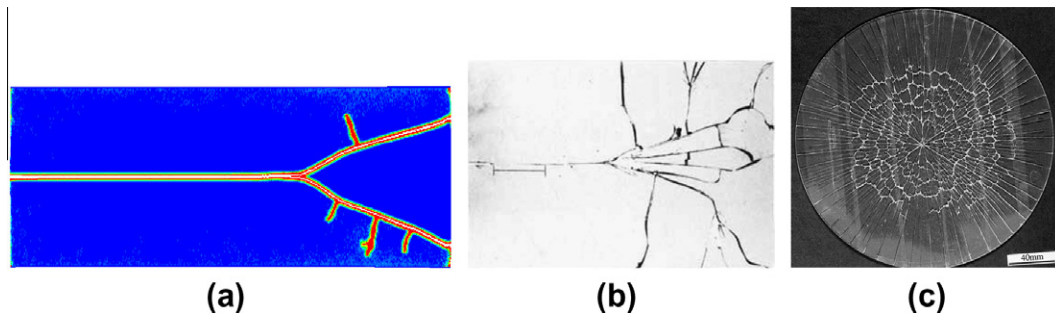
Fig. 11. Secondary cracking events in peridynamics and experiments: (a) peridynamic crack path with damage-independent model, $\delta \approx 1$ mm, $\sigma = 14$ MPa, (b) experimental secondary cracking induced by superposed stress waves (from [3]), (c) experimental circumferential and radial cracking by impact (from [6]).

damaged material, one modifies (stiffens) the micromoduli of bonds connecting nodes on or close to the crack surfaces. This later effect was investigated in the context of molecular dynamics in [23]. Here we obtain a similar dynamic instability to that observed in [23] but with a different concept, and with a continuum model. Buehler and Gao [23] do not discuss crack branching, they only focus on the instability of a single crack.

4.2. Secondary cracks induced by reflected waves

In this section we follow the crack propagation event after the main cracks reach the free edges on the right-hand side. In Fig. 10, the elastic strain energy evolution in time is illustrated side-by-side with the corresponding damage maps which show the crack patterns from 13 μs to 75 μs. The numerical model used in these simulations has the horizon of $\delta \approx 1$ mm and a tensile loading of 23 MPa is used. For each set of figures the contour legends are the same. At 13 μs, the strain energy is concentrated near the crack-tip and we notice the first crack branching attempt. The lower crack branch arrests soon after its initiation and only the upper one continues to propagate. At 21 μs the strain energy is concentrated again around the crack-tip and a second crack branching happens. Before the branches reach the right free edge, the elastic waves mainly propagate along and ahead of the branching directions (see 31 μs of Fig. 10). After the crack paths reach the free edge, the elastic waves are reflected and concentrate around the faces of the crack paths (see 60 μs of Fig. 10). Secondary cracks, almost perpendicular to the existing cracks directions, appear and propagate from these areas of highly concentrated strain energy (see 75 μs of Fig. 10). Both sets of plots in Fig. 10 also show how the cracks curve or arrest due to the interactions with the reflected waves. In [20,21] detailed studies of the stress wave interaction with the propagating cracks are given. The influence of the stress waves on curving and arrest of cracks is analyzed in [20] and the effects on the crack propagation speed are shown in [21]. We note that similar secondary crack patterns are observed with the peridynamic simulation of brittle target fragmentation at impact (see [24]) and are also observed in experiments of dynamic brittle fracture in [3,6] (see Fig. 11b and c). The secondary cracks observed from these peridynamic computations with the damage-dependent s_0 model are also obtained with the damage-independent s_0 model seen in Fig. 11a.

5. Conclusions

The dynamic brittle fracture phenomenon is a very sensitive and unstable event. Many experimental results in dynamic brittle fracture have shown certain types of asymmetry in the crack path under symmetric problem setups [1–5]. In this paper, we showed that one source of symmetry-breaking in a computational model that uses a perfectly symmetric geometrical grid about the pre-crack line was the way in which the lists of neighbors for some node and its symmetric about the pre-crack line are put together. The break of symmetry in these lists results in operations (sums to compute nodal forces) that are not performed in the same order between symmetric pairs of nodes about the line of fracture. As a consequence, round-off errors build-up in a non-symmetric way and because of this the symmetry of the crack branches is broken.

We also investigated the effect of strengthening of the peridynamic bonds that connect points that have already sustained some damage, like those between nodes near or on the crack faces. This was enforced by increasing the critical relative elongation value for peridynamic bonds between such nodes in a proportional manner to the local damage value. The results show that symmetry-breaking in crack branching is dramatically enhanced by this process, and that the dynamic crack-path instability is significant. This effect is new and it shows that there is yet another process that can influence the instability of dynamic crack propagation, in place of, or in addition to, using hyperelasticity around the crack-tip, as it was done in some recent atomistic simulations of dynamic fracture. In peridynamics, modifying the micromoduli (stiffness) for bonds in the damaged zone in a similar manner with that used here for the critical relative elongation parameter will likely have a similar effect on the dynamic crack-path instability.

The numerical investigations also showed that successive branching events and secondary cracks are predicted by the peridynamic formulation with minimum input data (bulk modulus and density, and fracture energy) and without the aid of any ad-hoc criteria or conditions. As the stress level around the crack-tip increases, a propagating crack can depart from its original straight trajectory and it can curve or split into two or more branches. Beyond certain stress levels reached before the pre-crack starts to run, branching cascades (successive branching events) appear. The direction of propagation of these crack paths, and even their arrest, are critically affected by the stress waves moving through the material. Furthermore, once the crack paths reach the free edges of the sample, the peridynamic simulations indicate that the formation of secondary or "circumferential" cracks (starting along the faces of the primary cracks, at ∼90° angles from these) is induced by the reflected stress waves. Similar behavior of successive branching and secondary cracks are observed in dynamic brittle fracture experiments [1,3,6].

In conclusion, peridynamics, a nonlocal continuum model, can correctly reproduce important characteristic features of dynamic brittle fracture: crack branching, crack-path instability, symmetry-breaking of crack paths, successive branching, and secondary cracks. We have shown that peridynamics correctly predicts behavior of these fracture processes, and that the mechanisms that control them are mainly the ways in which strain energy is delivered into the fracture zone.

Acknowledgements

References

[1] Bowden FP, Brunton JH, Field JE, Heyes AD. Controlled fracture of brittle solids and interruption of electrical current. Nature 1967;216:38–42.
[2] Ramulu M, Kobayashi AS. Mechanics of crack curving and branching – a dynamic fracture analysis. Int J Fract 1985;27:187–201.
[3] Ravi-Chandar K, Knauss WG. An experimental investigation into dynamic fracture: IV. On the interaction of stress waves with propagating cracks. Int J Fract 1984;26:189–200.
[4] Ramulu M, Kobayashi AS, Kang BSJ, Barker DB. Further studies on dynamic crack branching. Exp Mech 1983;23:431–7.
[5] Ravi-Chandar K, Knauss WG. An experimental investigation into dynamic fracture: III. On steady-state crack propagation and crack branching. Int J Fract 1984;26:141–54.
[6] Hull D. Fractography. Cambridge University Press; 1999.
[7] Belytschko T, Chen H, Xu J, Zi G. Dynamic crack propagation based on loss of hyperbolicity and a new discontinuous enrichment. Int J Numer Methods Engng 2003;58:1873–905.
[8] Abraham FF, Brodbeck D, Rudge WE, Xu X. Instability of fracture – a computer-simulation investigation. Phys Rev Lett 1994;73:272–5.
[9] Abraham FF, Brodbeck D, Rudge WE, Xu X. A molecular-dynamics investigation of rapid fracture mechanics. J Mech Phys Solids 1997;45:1595–619.
[10] Marder M, Gross S. Origin of crack-tip instabilities. J Mech Phys Solids 1995;43:1–48.
[11] Xu XP, Needleman A. Numerical simulations of fast crack growth in brittle solids. J Mech Phys Solids 1994;42:1397–434.
[12] Camacho GT, Ortiz M. Computational modelling of impact damage in brittle materials. Int J Solids Struct 1996;33:2899–938.
[13] Ortiz M, Pandolfi A. Finite-deformation irreversible cohesive elements for three-dimensional crack-propagation analysis. Int J N umer Methods Engng 1999;44:1267–82.
[14] Rabczuk T, Belytschko T. Cracking particles: a simplified meshfree method for arbitrary evolving cracks. Int J Numer Methods Engng 2004;61:2316–43.
[15] Zhou F, Molinari JF. Dynamic crack propagation with cohesive elements: a methodology to address mesh dependency. Int J Numer Methods Engng 2004;59:1–24.
[16] Song J, Areias PMA, Belytschko T. A method for dynamic crack and shear band propagation with phantom nodes. Int J Numer Methods Engng 2006;67:868–93.
[17] Song JH, Wang H, Belytschko T. A comparative study on finite element methods for dynamic fracture. Comput Mech 2008;42:239–50.
[18] Zhou SJ, Lomdahl PS, Thomson R, Holian BL. Dynamic crack processes via molecular dynamics. Phys Rev Lett 1996;76(13):2318–21.
[19] Silling SA. Reformulation of elasticity theory for discontinuities and long-range forces. J Mech Phys Solids 2000;48:175–209.
[20] Ha YD, Bobaru F. Studies of dynamic crack propagation and crack branching with peridynamics. Int J Fract 2010;162:229–44.
[21] Ha YD, Bobaru F, Parks ML. Predictive models for dynamic fracture in brittle materials: the peridynamic solution, in preparation.
[22] Field JE. Brittle fracture: its study and application. Contemp Phys 1971;12(1):1–31.
[23] Buehler MJ, Gao H. Dynamical fracture instabilities due to local hyperelasticity at crack tip. Nature 2006;439(19):307–10.
[24] Parks ML, Lehoucq RB, Plimpton SJ, Silling SA. Implementing peridynamics within a molecular dynamics code. Comput Phys Commun 2008;179(11):777–83.
[25] Silling SA. Fragmentation modeling with EMU. Technical report, Computational Physics Department, Sandia National Laboratories, Albuquerque, New Mexico, USA; 2005.
[26] Döll W. Investigations of the crack branching energy. Int J Fract 1975;11:184–6.
[27] Silling SA, Askari E. A meshfree method based on the peridynamic model of solid mechanics. Comput Struct 2005;83:1526–2535.
[28] Bobaru F, Yang M, Alves LF, Silling SA, Askari E, Xu J. Convergence, adaptive refinement, and scaling in 1D peridynamics. Int J Numer Methods Engng 2009;77:852–77.
[29] Gerstle W, Sau N, Silling S. Peridynamic modeling of plain and reinforced concrete structures. In: Conference paper in 18th international conference on structural mechanics in reactor technology (SMiRT 18), Beijing, China, SMiRT18-B01-2; 2005.
[30] Gerstle W, Sau N, Silling S. Peridynamic modeling of concrete structures. Nucl Engng Des 2007;237:1250–8.
[31] Silling SA, Epton M, Weckner O, Xu J, Askari E. Peridynamic states and constitutive modeling. J Elast 2007;88:151–84.
[32] Bobaru F. Influence of van der Waals forces on increasing the strength and toughness in dynamic fracture of nanofiber networks: a peridynamic approach. Model Simul Mater Sci 2007;15:397–417.
[33] Hairer E, Lubich C, Wanner G. Geometric numerical integration illustrated by the Strmer/Verlet method. Acta Numer 2003:1–51.